A Microwave Model for High Electron Mobility Transistors

Varakorn Kasemsuwan and Mahmoud A. El Nokali *Senior Member, IEEE*

***Abstract*— In this paper, the authors present a high-frequency model for the high electron mobility transistor (HEMT). The model includes the distributed effects in the channel of the device through two newly developed wave equations in the linear and saturation regimes. The equations are solved taking into account the electric fields along and perpendicular to the flow of the current. The Y and S parameters are derived and the theoretical predictions of the model are compared with the experimental data and shown to be in good agreement over a wide range of frequencies.**

I. Introduction

THE HIGH electron mobility transistor (HEMT) has received considerable interest for both microwave and high-speed digital circuit applications. Numerous quasi-static models that are valid in low- and mid-frequency ranges have been published [1]–[5]. The nonquasi-static approach has been used by several authors to account for the distributed effect at high frequencies. In [6] the channel of the HEMT is modeled as a transmission line by using a number of *RC* cascaded stages. The accuracy of these results is a function of the number of stages used in the model. An interesting question arises as to the optimal number of cascaded stages needed at different frequencies of operation. Even though the model takes into account the effects of both the two-dimensional dectron gas (2DEG) and the neutral donors in AlGaAs, it fails to account for the parallel conduction in the AlGaAs layer. An ac model developed by deriving the device wave equation and by solving it using a frequency power series method introduced by [9] is shown in [7] and [8]. The wave equation in [7], [8] is derived by assuming that the 2DEG capacitance C_g and the threshold voltage V_T are constants rather than being spatially dependent. In addition, this model considers the effect of the 2DEG charges while ignoring the influence of the parasitic MESFET.

In this paper, two new wave equations for HEMT are developed for both the linear and the saturation regimes. The equations account for the contribution from both the vertical and lateral electric fields through the solution of a quasi-two-dimensional (2–D) Poisson's equation in the high field region of the channel. A finite difference method is used to solve the wave equations and the ac currents and voltages are obtained everywhere along the channel. The Y and S parameters are derived from the model and compared with the experimental data available in the literature.

Manuscript received July 8, 1996; revised November 21, 1996.

The authors are with the Electrical Engineering Department, University of Pittsburgh, Pittsburgh, PA 15261 USA.

Publisher Item Identifier S 0018-9480(97)01717-1.

II. Device Wave Equations

In this section, two new wave equations are developed for the HEMT in the linear and saturation regimes. In the linear regime, the wave equation is obtained by combining the charge and velocity expressions with the continuity equation. In the saturation regime, the channel is divided into two regions as shown in Fig. 1, the low field and the high field regions. In the low field region, the wave equation is similar to that used in the linear regime. In the high field region, the wave equation is derived by combining the continuity equation with the quasi-2-D Poisson's equation.

A. Linear Regime

In HEMT, there are basically two types of mobile carriers that contribute to current conduction. The first type results in the 2DEG charges at the interface formed between the wider bandgap and the smaller bandgap materials, while the second type leads to the parasitic MESFET charges induced in the undepleted wider bandgap material. To take into account the effect of these two charges, the authors propose to use the following expression suggested in [10]:

$$n_{si}(y) = \sum_{i=1}^{2} \frac{n_{soi}}{A_i + B_i \exp\left[-C_i(D_i + v_{GS} - v_{Ci}(y)\right]} \quad (1)$$

where n_{so} is the maximum electron concentration, $v_C(y, t)$ is the potential along the channel, v_{GS} is the applied gate voltage, $i = 1, 2$ refers to the 2DEG and AlGaAs components of charge, respectively. The constants A, B, C, and D are used to fit (1) to the charge resulting from an exact numerical simulation.

The current equation in HEMT is written as

$$i_{Di}(y, t) = qW n_{si}(y, t)\, V_i(y, t) \quad (2)$$

where q is the electron charge, W is the gatewidth, and $V_i(y, t)$ is the electron velocity given by

$$V_i(y, t) = \mu_{oi} \frac{E_i(y, t)}{1 + \dfrac{E_i(y, t)}{E_{1i}}} \quad (3)$$

where E_{1i} is given as

$$E_{1i} = \frac{E_{Ci}}{\left(\dfrac{\mu_{oi} E_{Ci}}{v_{\text{sati}}}\right) - 1}.$$

μ_o, $E(y, t)$, and E_C are the low field mobility, the electric field along the channel and the critical electric field, respectively, and $v_{\rm sat}$ refers to the peak velocity of the stationary velocity field relation.

The continuity equation is given by

$$\frac{\partial i_{Di}(y, t)}{\partial y} = -qW \frac{\partial n_{si}(y, t)}{\partial t} \tag{4}$$

where t denotes time.

The wave equation for a device operating in the linear regime is derived by combining (1)–(4). The model uses the charge expression suggested in [10] due to its inherent advantages. First, (1) accounts for the nonlinearity in the 2DEG charge which extends its validity to a wide range of gate voltages. The equation is also both differentiable and integrable resulting in an analytical expression for the current voltage characteristic. In addition, (1) accounts for the 2DEG charge concentration as well as the parallel conduction in the AlGaAs layer. In terms of ac analysis, (1) allows for the extraction of the small signal components for both the 2DEG and the parasitic MESFET in a unified manner.

By combining (1)–(4) and expressing each current and voltage term as the sum of dc and ac components, e.g., $i_{Di}(y, t) = I_{Di} + i_{di}(y)e^{j\omega t}$, one can obtain the device wave equation for an electric field less than E_{1i}, as

$$\frac{d^2}{dy^2}\left[\frac{v_i(y)}{K_{1i}}\right] = -jw\frac{K_{2i}v_i(y)}{\mu_{oi}K_{1i}^2} \tag{5}$$

where

$$\begin{aligned} v(y) &= v_{gs} - v_c(y) \\ K_{1i} &= A_i + B_i e^{-C_i\,[D_i + V_i(y)]} \\ K_{2i} &= -C_i\,B_i e^{-C_i[D_i + V_i(y)]}. \end{aligned}$$

Equation (5) is a nonlinear second-order differential equation which includes the ac variable $v_i(y)$ and the dc variable $V_i(y)$, through K_{1i} and K_{2i}.

B. Saturation Regime

As the device is driven into saturation, the channel can be divided into a low field and a high field region as shown in Fig. 1. The transition between the two regions occurs at the point where the electric field is equal to the critical field E_c. In Region I (low field), the gradual-channel approximation applies and the wave equation is given by (5). In Region II (high field), the mobile carriers are assumed to move with a constant speed equal to the saturation velocity $v_{\rm sat}$.

The continuity equation in the saturation region is written as

$$\frac{\partial i_{Di}(y, t)}{\partial y} = -\frac{1}{v_{\rm sati}}\frac{\partial i_{Di}(y, t)}{\partial t}. \tag{6}$$

The mobile carriers in Region II are assumed to be spread over an average width d_{s1} for the 2DEG conduction and over d_{s2} for the parasitic MESFET conduction. For each conduction mechanism, a rectangular Guassian surface $ABCD$ is assumed to embrace the charges responsible for that conduction.

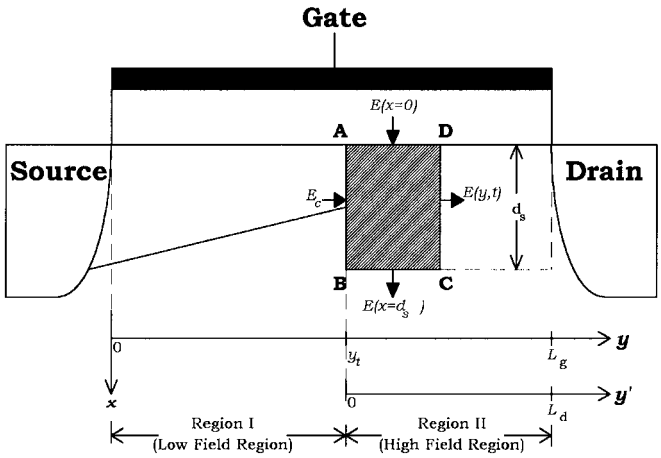

Fig. 1. Device cross section in the saturation regime.

Applying Gauss's law to the sides of rectangle $ABCD$ yields

$$\begin{aligned} &\int_0^{d_{si}} [E_i(y) - E_{Ci}]\,dx + \int_0^y [E(x = d_{si}) - E(x = 0)]\,dy \\ &\quad = -\frac{q}{\varepsilon_i}\int_0^y \int_0^{d_{si}} [n_{si}(y, t) - N_{Di}]\,dx\,dy \end{aligned} \tag{7}$$

where N_{Di} is the doping concentration and E_{Ci}, $E(x = 0)$, $E(x = d_s)$, and $E(y, t)$ are the electric fields perpendicular to the boundaries AB, AD, BC, and CD, respectively. $i = 1$ refers to quantities related to 2DEG conduction and $i = 2$ to AlGaAs conduction.

By differentiating (7) with respect to y with $dE_i(y, t)/dy$ replaced by $-d^2v_{Ci}(y, t)/dy^2$ and using the fact that the charge attributed to the vertical electric field is estimated by (1), one can obtain

$$\begin{aligned} &\frac{d^2v_{Ci}(y, t)}{dy^2} + \frac{qn_{soi}}{\varepsilon_i\,d_{si}\,\{A_i + B_i e^{-C_i[D_i + v_{GS} - v_{Ci}(y, t)]}\}} \\ &\quad = -\frac{qN_{Di}}{\varepsilon_i} + \frac{i_{Di}(y, t)}{\varepsilon_i\,d_{si}Wv_{\rm sati}}. \end{aligned} \tag{8}$$

Equation (8) is a quasi-2-D Poisson's equation that is used with the continuity (6) to model the device in the high field region of the channel. The average spreading width d_{s1} of the 2DEG charge is chosen such that the calculated value of the dc current provides a good fit to the experimental data. The average spreading width of the parasitic MESFET charge is assumed to be equal to the average undepleted widths in the AlGaAs layer, i.e., $d_{s2} = [W(L_d) + W(L_g)]/2$ where $W(L_d)$ is the width of the undepleted AlGaAs at the start of the high field region and $W(L_g)$ is the width at the end of the region [11].

Extracting the ac components from (6) and (8) yields

$$\frac{di_{di}(y)}{dy} = -j\omega\frac{i_{di}(y)}{v_{\rm sati}} \tag{9a}$$

$$\frac{d^2v_i(y)}{dy^2} + [v_{gs} - v_i(y)]\frac{qn_{soi}K_{2i}}{\varepsilon_i\,d_{si}K_{1i}^2} = -\frac{i_{di}(y, t)}{\varepsilon_i d_{si}Wv_{\rm sat}}. \tag{9b}$$

Rearranging (9a) and (9b) results in

$$\frac{d^2v_i(y)}{dy^2} + [v_{gs} - v_i(y)]\frac{qn_{soi}K_{2i}}{\varepsilon_i d_{si}K_{1i}^2} = -\frac{j}{\omega\varepsilon_i d_{si}W}\frac{di_d(y)}{dy}. \tag{10}$$

Equation (10) is the wave equation in the high field region of the channel while (5) is its counterpart in the low field region.

III. Solution of the New Device Wave Equations

In this section, the device wave equations in both Regions I and II will be solved. The small signal gate to channel potential $v(y)$ and small signal current $i_d(y)$ will be calculated along the channel.

A. Solution in the Linear Regime

The channel of the device is divided into n sections where y_0 and y_n represent the source and the drain ends, respectively.

By defining $\zeta(y) = v(y)/K_1(y)$ and $\psi(y) = d\zeta(y)/dy$, one can rewrite (5) as

$$\frac{d\psi(y)}{dy} = -jw\frac{K_2(y)\zeta(y)}{\mu_o K_1(y)}. \tag{11}$$

Expanding $\psi(y)$ and (11) using a Tayor series yields

$$\zeta(y_k) = \frac{v(y_0)}{K_1(y_0)} + h\sum_{j=0}^{k-1}\psi(y_j) \tag{12a}$$

$$\psi(y_k) = -\frac{i_d(y_0)}{K_3} - \frac{j\omega h}{\mu_o}\sum_{j=0}^{k-1}\frac{K_2(y_j)\zeta(y_j)}{K_1(y_j)} \tag{12b}$$

where y_k refers to a particular location along the channel, $1 \le k \le n$, $\zeta(y_0)$, and $\psi(y_0)$ are evaluated at the source end and given by $v(y_0)/K_1(y_0)$ and $-i_d(y_0)/K_3$, respectively, and h denotes the size of a step.

By substituting $\psi(y_0)$ and $\zeta(y_0)$ into (12a) and (12b), one can obtain $\zeta(y_1)$ and $\psi(y_1)$ as functions of $v(y_0)$ and $i_d(y_0)$. By repeating the above step, it is obvious that one can write $\zeta(y_k)$ and $\psi(y_k)$ as functions of $v(y_0)$ and $i_d(y_0)$, such as

$$\begin{aligned}\psi(y_k) &= av(y_o) + bi_d(y_o)\\ \zeta(y_k) &= cv(y_o) + di_d(y_o).\end{aligned} \tag{13}$$

However, since $v(y_k) = \zeta(y_k)K_1(y_k)$ and $i_d(y_k) = -K_3\psi(y_k)$, one can rewrite (13) as

$$v(y_k) = a_k v(y_o) + b_k i_d(y_o) \tag{14a}$$

$$i_d(y_k) = c_k v(y_o) + d_k i_d(y_o) \tag{14b}$$

where $a_k = -aK_3$, $b_k = -bK_3$, $c_k = cK_1(y_k)$, and $d_k = dK_1(y_k)$.

B. Solution in the Saturation Regime

Once a device is biased in the saturation regime the point along the channel where the electric field is equal to E_c moves toward the source terminal. This phenomenon is known as the channel-length modulation effect and results in a channel that is divided into two regions: the low field region $0 < y < L_g - L_d$ and the high field region $L_g - L_d < y < L_g$. The analysis performed in the linear regime is applicable to the low field region and (14) is valid in this region of the channel. The two small signal variables $v(y_k)$ and $i_d(y_k)$ in the high field region of the channel are found in a way that satisfies the continuity of these variables at the transition point y_t.

There are two steps involved in solving for $v(y_k)$ and $i_d(y_k)$ in the high field region of the channel. First, the Runge–Kutta algorithm of order 4 is applied to (9a) to obtain the small signal current $i_d(y_k)$. The small signal current at the transition point $i_d(y_t)$ which is used as boundary condition for the algorithm is obtained from the solution of the wave equation in the low field region of the channel. Then the Runge–Kutta–Nyström algorithm is applied to (9b) to obtain the small signal voltage $v(y_k)$. The boundary values for $v(y_t)$ and its derivative $v'(y_t)$ result from the solution of the wave equation in the low field region. By following these two steps, one can again write $v(y_k)$ and $i_d(y_k)$ similar to (14a) and (14b) with a new set of a_k, b_k, c_k, and d_k.

It is important to emphasis the fact that $v_i(y)$ in (10) and $\zeta(y_k)$, $\psi(y_k)$ in (12a) and (12b) are functions of the dc channel potential $V_C(y)$ through $K_1(y)$ and $K_2(y)$. Therefore, $v(y_k)$ and $i_d(y_k)$ will also be functions of the dc channel potential which needs to be computed.

In calculating the dc potential in the low field region of the channel, one can obtain the relationship between the distance y to the dc channel potential V_y along the channel by combining (1)–(3) as

$$\begin{aligned}y = &\left(\frac{qW\,n_{so}\mu_o}{AI_D} - \frac{1}{E_1}\right)V_y\\ &- \frac{qWn_{so}\mu_o}{ACI_D}\ln[A + Be^{-C(D+V_{GS}-V_y)}].\end{aligned} \tag{15}$$

The dc current I_D is calculated at a given gate voltage and drain voltage as outlined in [10]. The Newton–Raphson method is used to find the dc potential along the channel in (15) and it has been found that the solution converges after a few iterations.

In the high field region, the Runge–Kutta–Nyström is used to solve the dc quasi-2-D equation which is obtained by extracting the dc component from (8). The solution assumes that the dc channel potential and the lateral electric field at the start of the region $y = y_t$ are equal to V_{DSAT} and E_c, respectively.

IV. Calculation of the Y and S Parameters

In this section, the intrinsic Y-parameters for HEMT operating in the linear and saturation regimes will be calculated first. Equation (14), which is valid for a device operating in both regimes, will be used as the key equation in the derivation. The extrinsic Y-parameters will be computed by adding the

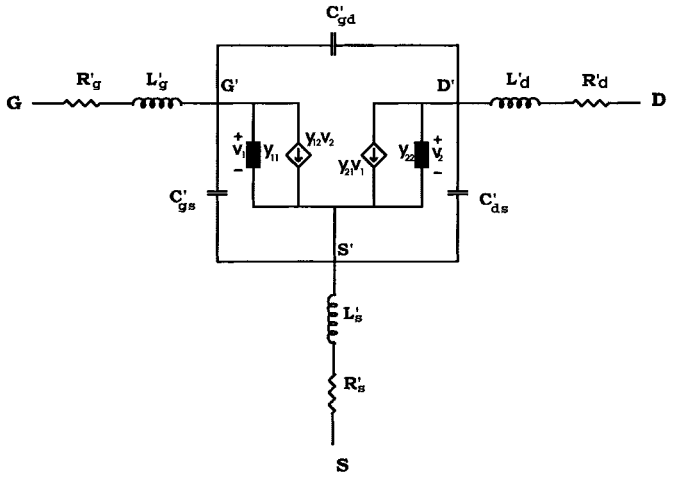

Fig. 2. Small signal equivalent circuit of HEMT's.

extrinsic elements to the intrinsic model and are then converted to find the S-parameters.

The intrinsic Y-parameters for HEMT can be found using the following definitions:

$$y_{11} = \left.\frac{i_g}{v_{gs}}\right|_{v_{ds}=0} = \left.\frac{i_d(y_o) - i_d(y_n)}{v_{gs}}\right|_{v_{ds}=0}$$
$$y_{21} = \left.\frac{i_d}{v_{gs}}\right|_{v_{ds}=0} = \left.\frac{i_d(y_n)}{v_{gs}}\right|_{v_{ds}=0}$$
$$y_{12} = \left.\frac{i_g}{v_{ds}}\right|_{v_{gs}=0} = \left.\frac{i_d(y_o) - i_d(y_n)}{v_{ds}}\right|_{v_{gs}=0}$$
$$y_{22} = \left.\frac{i_d}{v_{ds}}\right|_{v_{gs}=0} = \left.\frac{i_d(y_n)}{v_{ds}}\right|_{v_{gs}=0}. \tag{16}$$

To find y_{11}, y_{21} and y_{12}, y_{22}, the boundary conditions, according to (16), are $v(y_o) = v(y_n) = v_{gs}$ and $v(y_o) = 0$, $v(y_n) = -v_{ds}$, respectively.

Substituting the boundary condition for computing y_{11}, y_{21} in (14a) and (14b) yields

$$i_d(y_0) = v_{gs}\left(\frac{1-a_n}{b_n}\right) \tag{17a}$$
$$i_d(y_n) = c_n v_{gs} + d_n\left(\frac{1-a_n}{b_n}\right) v_{gs} \tag{17b}$$

where a_n, b_n, c_n, and d_n are frequency dependent.

Applying (17a) and (17b) to the definition of y_{11} and y_{21} appearing in (16), one gets

$$y_{11} = \left(\frac{1-a_n}{b_n}\right) - c_n - d_n\left(\frac{1-a_n}{b_n}\right)$$
$$y_{21} = c_n + d_n\left(\frac{1-a_n}{b_n}\right). \tag{18}$$

By following the steps previously outlined with the boundary condition for computing y_{12} and y_{22}, one can obtain y_{12} and y_{22} as

$$y_{12} = \frac{d_n - 1}{b_n}$$
$$y_{22} = -\frac{d_n}{b_n}. \tag{19}$$

The admittance parameters calculated above are applicable to both the 2DEG and the parasitic MESFET conduction. To obtain the total value of each Y-parameter, one needs to add its two components.

The extrinsic Y-parameters are obtained from a straightforward circuit analysis by augmenting the intrinsic equivalent circuit for the device with the parasitic elements as shown in Fig. 2. Three of the elements represent pad-to-pad capacitances while the other six elements represent bulk resistances and the inductances associated with the bond wires used to connect the device to the fixture. The pad-to-pad capacitances result from the change of charges with the potentials on the pads and are functions of the device geometry.

On the other hand, if the two-port is described by the incident and reflected voltages at each port then the device can be described by the scattering parameters using a parameter conversion table [12].

TABLE I
PHYSICAL PARAMETERS

	Device 1	Device 2
N_{D2} [ea/cm^3]	1.2×10^{18}	1.76×10^{18}
d_1 [Å]	350	480
d_i [Å]	30	30
N_c [/cm^3]	7.05×10^{17}	7.05×10^{17}
E_d [eV]	0.05	0.05
x	0.25	0.2
Φ_B [eV]	1.1	1.1
ε_1 [F/cm]	1.10×10^{-12}	1.10×10^{-12}
ε_2 [F/cm]	1.09×10^{-12}	1.11×10^{-12}
D [/m^{2}J]	2.025×10^{34}	2.025×10^{34}
W [μm]	290	250
Lg [μm]	1	0.32

V. RESULTS AND DISCUSSION

In this section, the equations of the model are used to calculate the admittance and scattering parameters for the 2DEG's and parasitic MESFET's conduction. The theoretical predictions of the model are presented in Cartesian form rather than on a Smith chart since they will be compared with the experimental data published in Cartesian form by two independent research groups [5], [7]–[8]. Furthermore, a Smith chart can inadvertently hide poor fits which involve a frequency shift between the measured and theoretical data [5]. The physical parameters for the two devices used to produce the data are summarized in Table I where N_{D2}, d_1, d_i, N_C, E_d, x, Φ_B, ε_2, and D represent donor concentration, doped

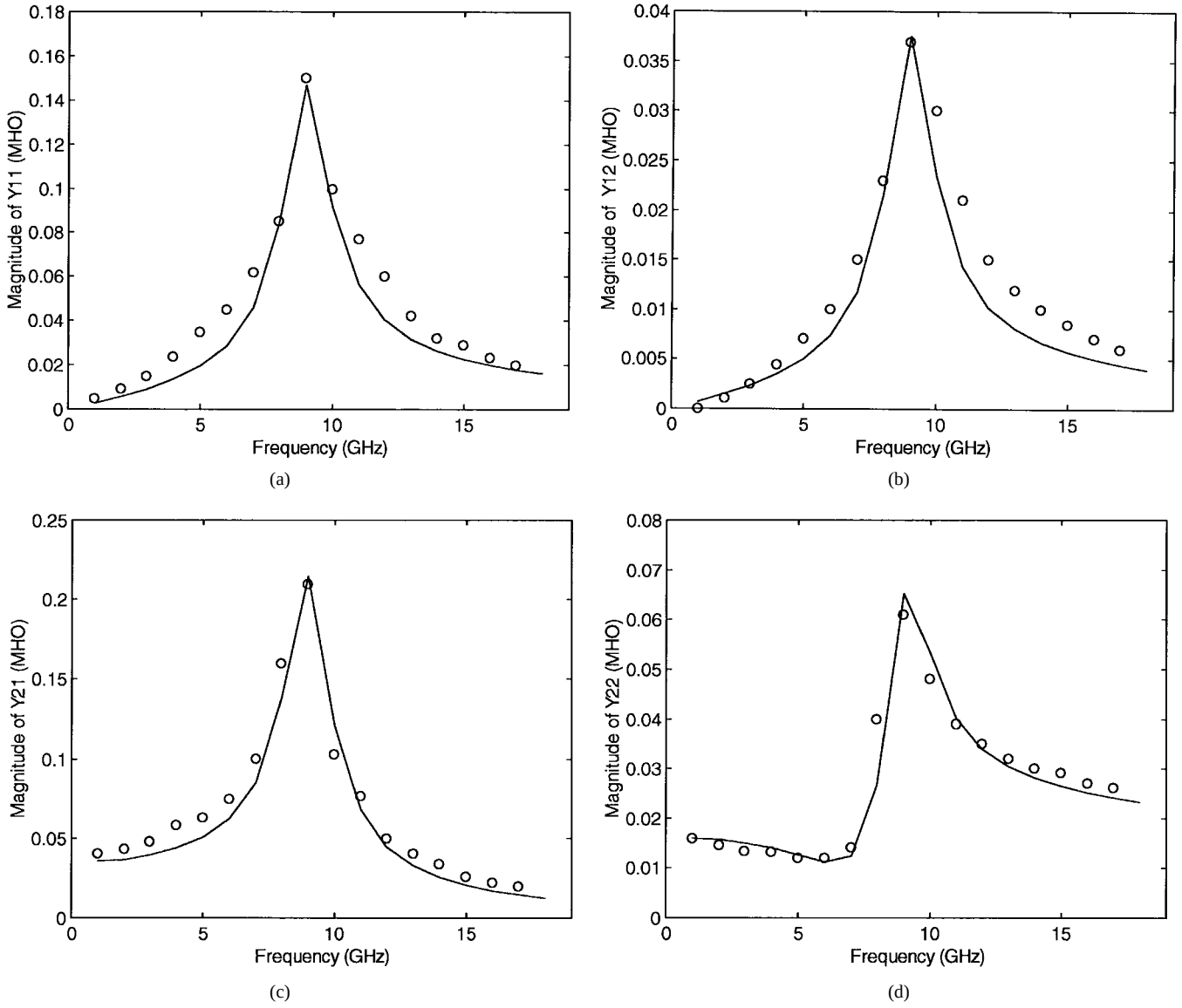

Fig. 3. Comparison of the magnitudes of the extrinsic admittance parameters resulting from 2DEG (-) and the experimental data (o) at $V_{GS} = 0.08$ and $V_{DS} = 0.5$ V for device #1: (a) y'_{11}, (b) y'_{12}, (c) y'_{21}, and (d) y'_{22}.

AlGaAs thickness, spacer thickness, effective density of states in AlGaAs conduction band, ionization energy in AlGaAs, Al mole fraction, Schottky barrier height, permittivity of AlGaAs, and density of states in the 2DEG channel, respectively. The authors' model contains two sets of parameters. The first set includes the constants A, B, C, D and are determined by fitting (1) to the exact numerical solution for the charge. The second set of parameters is listed in Table II and their values are found by matching the theoretical predictions of the model with the experimental results for the I–V characteristic of the device. Once determined, those parameters are kept constant in the calculation of the admittance and scattering parameters.

Two set of values were reported for the extrinsic parameters of device #1: the nonoptimized and the optimized values [7]. The authors have used the nonoptimized data to produce these results with the exception of the pad capacitances. Using the zero values reported for the capacitances would result in

TABLE II
MODEL PARAMETERS

	Device 1		Device 2	
	2DEG	n+ AlGaAs	2DEG	n+AlGaAs
A	1.014	0.001	1.043	0.001
B	10.710	4.439	3.816	6.834
C [V^{-1}]	5.799	5.519	5.642	3.262
D [V]	0.347	-0.725	1.60	1.00
d_{s1} [Å]	2600	-	3200	-
d_{s2} [Å]	-	66.05	-	33.5
μ_o [cm^2/V-s]	5800	600	5500	600
v_{sat} [Km/s]	190	80	165	80
E_c [KV/cm]	3.5	24.0	3.5	24.0
n_{so} [/cm^2]	1.01×10^{12}	2.61×10^{11}	6.65×10^{11}	8.45×10^{10}

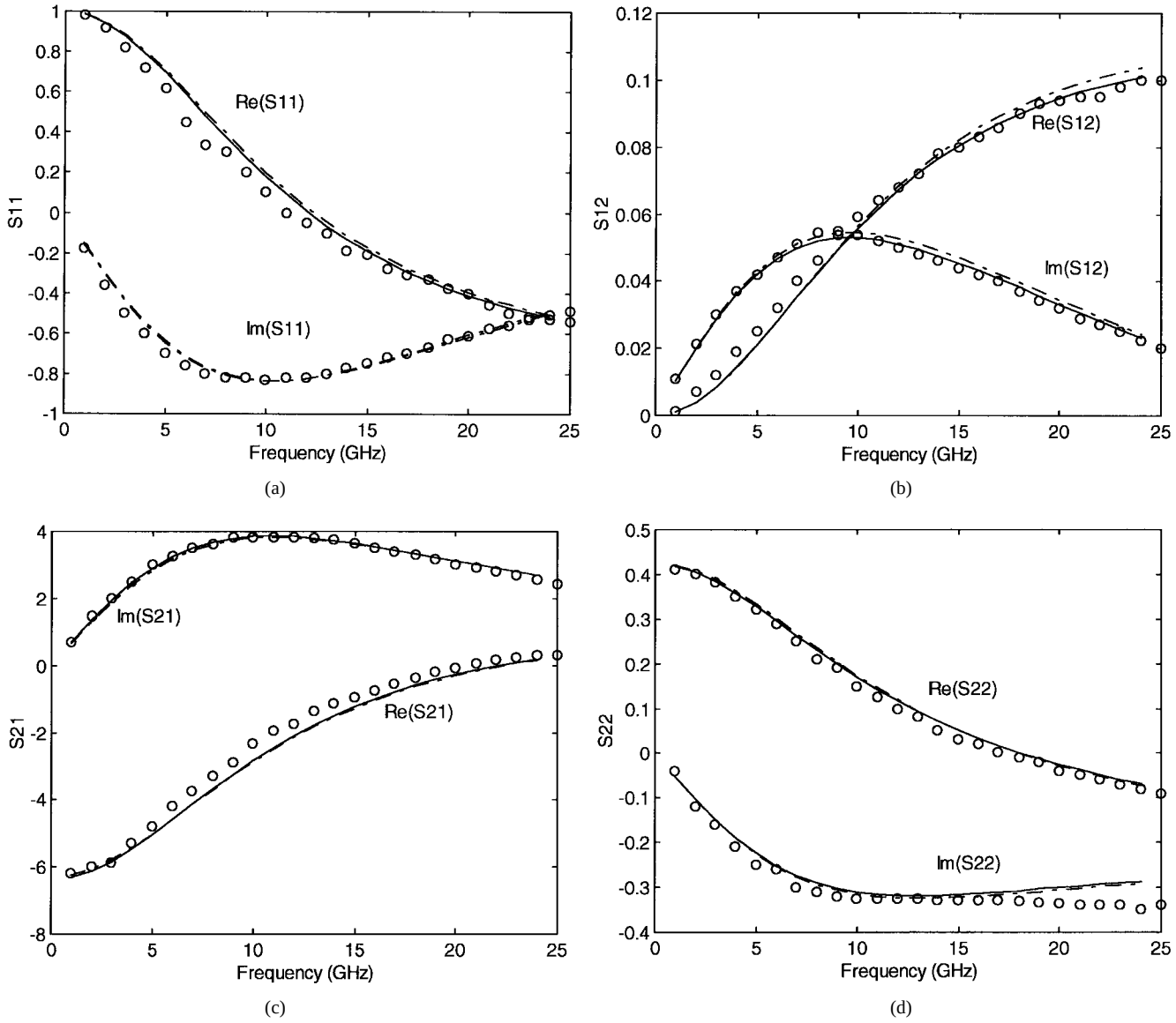

Fig. 4. Comparison of the real and the imaginary parts of the scattering parameters for 2DEG (-.), 2DEG plus MESFET (-) and experimental data (o) at $V_{GS} = -0.99$ and $V_{DS} = 2.0$ V for device #2: (a) S_{11}, (b) S_{12}, (c) S_{21}, and (d) S_{22}.

5%–10% error in the ac characteristic of the device. To reduce this error, the authors had two options: either to use different values for μ_o and $v_{\rm sat}$ than the ones reported in Table II or to optimize the value of the pad capacitances. By exercising the first option, the authors have found that if μ_o is changed to 5400 cm^2/V-s and $v_{\rm sat}$ is to become 215 Km/s, then the error from the ac analysis is reduced to within 5%. The adjustment, however, will corrupt the fit of the model with the measured I–V characteristic which is not advisable. The authors have elected the latter option by choosing C'_{gs}, C'_{ds}, and C'_{gd} to be 45, 39, and 41 fF in the model, respectively.

For device #2, the values of the parasitic parameters were empirically determined and are typical for the fabrication process and the device layout [5]. The authors have used the reported data with the exception of the pad capacitances which were selected to be 14, 0.005, and 53 fF for C'_{gs}, C'_{ds}, and C'_{gd}, respectively, using the same argument as before.

Fig. 3 compares the magnitude of the extrinsic Y-parameters resulting from the theoretical predictions of the model and the experimental data published in the literature [7] for device #1. The applied gate and drain voltages are 0.08 and 0.5 V, respectively. The maximum values of the different Y-parameters occur around the same frequency (9 GHz) as long as the extrinsic elements are not changed. It is well known that for the conduction in the AlGaAs channel to start, the gate voltage should exceed a critical value [11]. The critical gate voltage for device #1 is found to be 0.47 V which is higher than the applied gate voltage, thus resulting in no parasitic conduction.

Fig. 4 shows a comparison between the theoretically predicted real and imaginary parts of the scattering parameters for device #2 and the experimental data [5]. The gate and drain voltages are -0.99 and 2.0 V, respectively, and both conduction mechanisms occur in the saturation regime. The

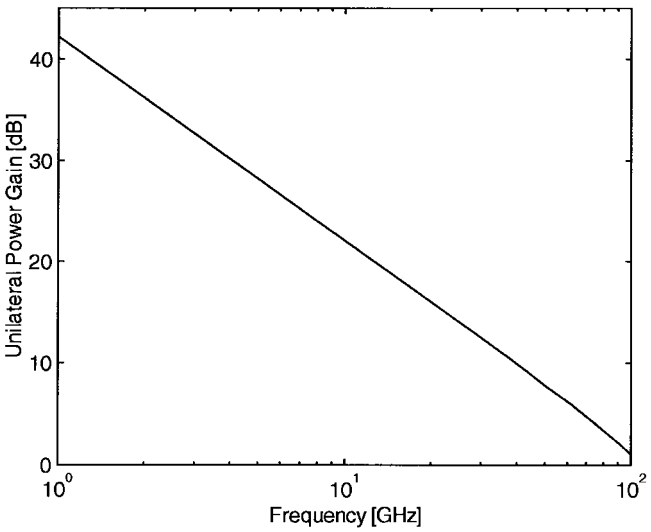

Fig. 5. Unilateral power gain for device #2 at $V_{GS} = -0.99$ and $V_{DS} = 2.0$ V.

critical gate voltage for device #2 is found to be -1.02 V which is lower than the applied gate voltage, thus suggesting the presence of the parasitic MESFET. However, it is clear that the contribution of the parasitic MESFET to the Y-parameters is negligible (1%–3% of total) compared to that resulting from the 2DEG.

It is instructive to note that the transconductance obtained from the dc model should be consistent with that resulting from the high-frequency characteristics. A check for this consistency for device #2 is performed by converting the S-parameters in Fig. 4 to the Y-parameters [12]. The transconductance would then correspond to y_{21} at zero frequency. For device #2, the transconductance for the gate and the drain voltages of -0.99 and 2.0 V, respectively, is calculated to be 275 mS/mm which agrees with the predictions of the dc model [10].

Several definitions of power gains are important in the design of an amplifier in the microwave range, e.g., transducer power gain, maximum available power gain, maximum stable power gain, etc. All of these gains are related to the scattering parameters. For instance, the unilateral power gain, which is the highest possible gain that the active two-port can achieve, can be expressed as [12]

$$U = \frac{1}{2}\frac{\left|\frac{S_{21}}{S_{12}} - 1\right|^2}{k\left|\frac{S_{21}}{S_{12}}\right| - \mathrm{Re}\left[\frac{S_{21}}{S_{12}}\right]} \tag{20}$$

where

$$k = \frac{1 + |\Delta S|^2 - |S_{11}|^2 - |S_{22}|^2}{2|S_{12}S_{21}|}$$
$$\Delta S = S_{11}S_{22} - S_{12}S_{21}.$$

Fig. 5 shows the plot of the unilateral power gain with the frequency for device #2. The maximum frequency of oscillation, at which the unilateral power gain is equal to one, is found to be 97.8 GHz for this bias condition.

At this stage, it is important to compare the approach that the authors used to derive the wave equation to that of [7], [8]. Although the two approaches use the same basic equations, namely the continuity and the current equations, they do differ in the expressions for the charge used. A linear charge expression similar to that used in the modeling MOSFET $\{n_s(y,t) = C_g[v_{GS} - V_T - v_C(y,t)]\}$ is assumed in [8]. In the derivation of the wave equation in [8], it is important to notice that the 2DEG gate capacitance C_g and the threshold voltage V_T were initially assumed constant and were later modified to the values reported in their dc model [13]. Since their expression for the charge is similar to the one used in the MOSFET the wave equation resulting from the analysis is, therefore, similar in form to the equations reported in [9] and [14] for both the JFET and the MOSFET. This similarity in form in [7], [8] allowed the use of the Fourier analysis method to obtain the intrinsic Y-parameters as functions of the operating frequency and the dc gate-to-channel potential in an analytical form.

To compare the authors' approach to the one used in [7], [8] it is instrumental to compare the authors' wave equations with [7], [8] in both regions of the channel for a device operating in saturation. In the low field region the wave equation of [7] which corresponds to (5) of the authors' analysis is

$$\frac{d^2}{dy^2}\{\mu[V(y) - V_T]v(y)\} = jwv(y). \tag{21}$$

Equation (21) is derived by assuming a constant gate capacitance for the device which is similar to the quasi-static approximation. However, to account for the distributed effects at high frequency, the nonquasi-static approach divides the device into sections where the quasi-static approximation can be used. If the length of the sections are allowed to approach zero then the gate capacitance at each point along the channel can be described as

$$C_g(y) = qn_{so}\frac{BCe^{C[D+V_{GS}-V_C(y)]}}{\{B + Ae^{C[D+V_{GS}-V_C(y)]}\}^2}. \tag{22}$$

The spatial dependence of the gate capacitance is accounted for through the dc channel potential $V_C(y)$. In the absence of an applied drain voltage at thermal equilibrium, the channel potential is zero and (22) reduces to the expression for the gate capacitance reported in [10].

In the high field region of the channel, the wave equation which corresponds to (10) of the authors' analysis is

$$\frac{d^2v(y)}{dy^2} = -\frac{j}{\omega\varepsilon d_s W}\frac{\partial i_d(y)}{\partial y}. \tag{23}$$

Comparing (10) and (23) reveals an extra term in (10). The term results from the contribution of the vertical electric field in the high field region of the channel which was neglected in [8]. In other words, whereas the model in [8] solved a one-dimensional Poisson's equation in the high field region of the channel, the authors are using a quasi-2-D Poisson's equation. By solving the ac quasi-2-D equation (10) the small signal parameters obtained are, therefore, accurate for both long and short channel devices.

It is instructive to note that this model can also be applied to the analysis of pseudomorphic HEMT's (pHEMT's). pHEMT's offer greater carrier confinement than HEMT's

which leads to a higher 2DEG charge concentration and less parasitic MESFET conduction. In addition, InGaAs has superior transport characteristic over GaAs. The principle of operation of the two devices is, however, similar and the data needed to produce the admittance and scattering parameters for pHEMT's would still be the numerical result for the charges and the measured I–V characteristics.

REFERENCES

[1] K. Lee, M. S. Shur, T. J. Drummond, and H. Morkoc, "Current-voltage and capacitance-voltage characteristics of modulation doped field effect transistors," *IEEE Trans. Electron Devices*, vol. ED-30, pp. 207–212, 1983.

[2] M. H. Weiler and Y. Aysli, "DC and microwave models for AlGaAs/GaAs high electron mobility transistor," *IEEE Trans. Electron Devices*, vol. ED-31, pp. 1854–1861, 1984.

[3] H. R. Yeager and R. W. Dutton, "Circuit simulation models for the high electron mobility transistor," *IEEE Trans. Electron Devices*, vol. ED-33, pp. 682–692, 1986.

[4] A. Eskandarian, "Determination of the small signal parameters of an AlGaAs/GaAs MODFET," *IEEE Trans. Electron Devices*, vol. 35, pp. 1793–1801, 1988.

[5] S. J. Mahon, D. J. Skellern, and F. Green, "A technique for modeling S-parameters for HEMT structures as a function of gate bias," *IEEE Trans. Microwave Theory Tech.*, vol. 40, pp. 1430–1440, 1992.

[6] D. H. Huang and H. C. Lin, "DC and transmission line models for a high electron mobility transistor," *IEEE Trans. Microwave Theory Tech.*, vol. 37, pp. 1361–1370, 1989.

[7] P. Roblin, S. Kang, A. Ketterson, and H. Morkoc, "Analysis of MODFET microwave characteristics," *IEEE Trans. Electron Devices*, vol. ED-34, pp. 1919–1928, 1987.

[8] P. Roblin, S. Kang, and H. Morkoc," Analytical solution of the velocity-saturated MOSFET/MODFET wave equation and its application to the prediction of the microwave characteristics of MODFET's," *IEEE Trans. Electron Devices*, vol. 37, pp. 1608–1621, 1990.

[9] V. Ziel and E. N. Wu, "High-frequency admittance of high electron mobility transistors (HEMT's)," *Solid State Electron*, vol. 26, pp. 753–754, 1983.

[10] H. Ahn and M. El Nokali, "An analytical model for high electron mobility transistors," *IEEE Trans. Electron Devices*, vol. 41, pp. 874–878, 1994.

[11] D. Delagebeandeuf and N. T. Linh, "Metal-(n) AlGaAs-GaAs two-dimensional electron gas FET," *IEEE Trans. Electron Devices*, vol. MTT-29, pp. 955–960, 1982.

[12] H. Beneking, *High Speed Semiconductor Devices.* London, U.K.: Chapman & Hall, 1994.

[13] H. Rohdin and P. Roblin, "A MODFET dc model with improved pinch off and saturation characteristics," *IEEE Trans. Electron Devices*, vol. ED-33, pp. 664–672, 1986.

[14] J. J. Paulos and D. A. Antoniadis, "Limitation of quasistatic capacitance models for the MOS transistor," *IEEE Trans. Electron Devices*, vol. ED-4, pp. 221–224, 1983.

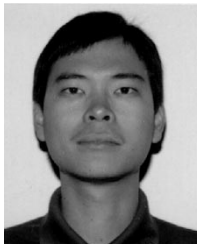

Varakorn Kasemsuwan was born in Bangkok, Thailand, on June 29, 1968. He received the B.S. degree in electrical engineering from the King Mongkut Institute of Technology Ladkrabang (KMITL), Bangkok, Thailand, and the M.S. degree in electrical engineering from the University of Pittsburgh, PA, in 1990 and 1993, respectively. He is currently working toward the Ph.D. degree at the University of Pittsburgh.

His research interests include modeling of SOI MOSFET's and HEMT's.

Mahmoud A. El Nokali (M'82–SM'85) was born in Alexandria, Egypt, on December 5, 1949. He received the B.S. degree in electrical engineering from Alexandria University in 1972, and the M.Eng. and Ph.D. degrees in electrical engineering from McGill University, Montreal, P.Q., Canada, in 1976 and 1980, respectively. His doctoral research dealt with the modeling and characterization of surface acoustic wave storage correlators.

After a year as a Post-Doctoral Fellow at McGill University, he joined the University of Pittsburgh, Pittsburgh, PA, as a Faculty Member of the Electrical Engineering Department where he is now Director of the Division of Continuing Engineering Education. His current research interests center on semiconductor device modeling, with special emphasis on short-channel MOSFET's, high-electron mobility transistors (HEMT's), SOI MOSFET's, and bipolar complimentary metal-oxide semiconductors (BiCMOS's).

Dr. El Nokali is a member of Eta Kappa Nu and Sigma Xi. He is the recipient of the 1986 Beitle-Veltri Teaching Award and the 1988 University of Pittsburgh Chancellor's Distinguished Teaching Award.